MUSE: Harnessing Precise and Diverse Semantics for Few-Shot Whole Slide Image Classification

Supplementary Material

1. Knowledge Base Generation Pipeline

1.1. Concept Decomposition

To consider the visual characteristics description of pathological images from multiple perspectives, we utilize the prompt to query GPT-4 [1] and summarize the diagnostic-related visual characteristics into four aspects: cellular morphology, tissue architecture, color-staining characteristics, and spatial-texture patterns. The prompt we used is: *You are an experienced pathologist. For the {dataset}, starting from visual features, what are four aspects that can be used for diagnosis? Summarize into four aspects*.

1.2. Example Generation

For each aspect, we query GPT-4 to generate 10 specific examples for each category, and these examples could guide the subsequent LLM to generate more accurate responses. The prompt we used in generating examples is: *From {perspective}, what are the characteristics of WSI images for {class name}? Please list 10 examples.* Specific examples for CAMELYON are presented in Section 9.

1.3. Multi-view Category Knowledge Base Construction

For each category in the dataset, we randomly select one example from each aspect as the description for that perspective, and combine these examples into a query prompt to query subsequent LLM. The query prompt is: *To supplement and systematize the description of {class name} in high-resolution imaging from four perspectives: {example from each perspective}. Please summarize it into a single paragraph.* In this prompt, *{example from each perspective}* is the example we selected for each perspective. For each category in every dataset, we generated 300 pathological descriptions using the above-mentioned generation procedure, forming the multi-view category knowledge base. We sampled one example per category from the generated knowledge base for each dataset, as shown in Table 1.

2. Implementation Details

In the DSR module, we set 8 query matrices as experts for fine-grained semantic processing, and a router network is employed to score these experts. The top-2 experts with the highest scores are selected for further processing. In the SVTI module, we retain only the top-20% patches with the highest attention scores for each head. In the SMMO component, we use the fine-grained semantic prior to retrieve the top-20 most similar text features from the knowledge base for subsequent semantic diversity optimization and enhancement. An Adam optimizer [2] with learning rate of 1×10^{-4} and weight decay of 1×10^{-5} is used for the model training. All the models are trained for 200 epochs with an early-stopping strategy. The batch size is set to 1. All the experiments are conducted with a single NVIDIA RTX 3090 GPU.

3. Training and Inference Strategy

During training, for each WSI bag, we generate fine-grained semantic priors using the SFSE module as follows: the DSR component first decomposes the raw semantic information into specialized representations, which are then utilized as fine-grained cues in the SVTI module. These fine-grained semantic priors serve as queries to retrieve relevant textual description features from the category-specific knowledge base. A stochastic optimization strategy is further adopted to leverage the retrieved semantic diversity. The detailed training procedure is outlined in Algorithm 1.

During inference, due to the absence of category priors, we input both the class names of the dataset and the test WSI into the SFSE module as well as the classifier to obtain the final prediction. The detailed algorithm is presented in Algorithm 2.

4. Details of Visualization

In the visualization of fine-grained semantics in the sample embedding space, we sample some textual description features from the category knowledge base to serve as raw semantics. We sample WSIs from the corresponding category and obtain the sample embeddings by averaging all patch features within the bags. Subsequently, we employ the SFSE module to perform fine-grained semantic modeling on these WSI bags, obtaining fine-grained semantic priors. We then use t-SNE [7] visualization to project sample embeddings, raw semantics, and fine-grained semantic priors into a shared embedding space for visual comparison.

In the comparison of text features retrieved by different samples, we sample several WSIs and obtain the corresponding fine-grained semantic priors using the SFSE module. These priors are then used as queries to retrieve relevant text features from the category knowledge base. Finally, we visualize the query, the candidate text features in the knowledge base, and the retrieved text features in a shared embedding space using t-SNE.

Table 1. Examples of sampled descriptions from the multi-view category knowledge base for each category within each dataset.

	Category	Description
CAMELYON	Normal	In high-resolution imaging, a normal lymph node exhibits uniform nuclear staining with homogeneous chromatin that lacks coarse granularity or heterogeneity. The vascular distribution is regular, featuring well-organized capillaries and small vessels without any signs of abnormal dilation or neovascularization. There are no non-physiological speckles, such as pigment deposits, debris, or staining artifacts, and the boundaries between different tissue regions show smooth transitions without abrupt changes or protrusions.
	Tumor	In high-resolution imaging of a metastatic lymph node, cellular crowding is evident with densely packed cells often forming clusters or sheets, indicative of significant tumor burden. Concurrently, irregular or distorted vascular structures are observed, showing signs of compression, dilation, or irregular branching of blood vessels, suggesting compromised microvascular integrity. Additionally, increased nuclear basophilia is noted, characterized by darker purple nuclei due to elevated DNA content in the tumor cells, reflecting their proliferative activity. Lastly, diffuse infiltration patterns are present, where tumor cells spread along existing tissue frameworks, displacing normal lymphoid architecture and disrupting the orderly arrangement of lymphocytes and other immune cells.
TCGA-NSCLC	LUAD	Lung adenocarcinoma exhibits a complex morphology that can be systematically described through high-resolution imaging. Notably, some cells display vacuolated or mucinous cytoplasmic changes, indicating alterations in cellular metabolism and possibly reflecting the presence of secretory activity. Additionally, the tumor often features fibrovascular cores within its papillary structures, which provide structural support and potentially contribute to the tumor's invasive capacity. Angiogenesis is another key feature, characterized by the presence of numerous, thin-walled blood vessels in the tumor stroma, which are crucial for tumor growth and survival. Lastly, there is significant heterogeneity in mucin content, with certain regions producing abundant mucin, while others show little or no production, suggesting diverse microenvironments and potential for different clinical behaviors.
	LUSC	In high-resolution imaging of lung squamous cell carcinoma, key features can be systematically described from four perspectives: Intercellular bridges manifest as visible desmosomal connections between tumor cells, indicating cellular cohesion. Polygonal tumor cells are characterized by well-defined, often angular shapes, reflecting the distinctive morphology of these neoplastic cells. The tumor-stroma interface exhibits heterogeneity, with irregular boundaries that highlight the complex interaction between the malignant cells and their microenvironment. Lastly, local variation in mitotic activity is evident, with hotspots of proliferating cells indicating areas of increased cellular division and potential for aggressive growth.
TCGA-BRCA	IDC	Invasive ductal carcinoma exhibits high cellular density with cells closely packed and minimal intervening stroma, leading to a crowded appearance. Ducts often show lumen formation with cellular debris accumulating within them. Surrounding these areas, peritumoral fibrosis is characterized by thickened fibrotic bands that encircle the invasive tumor regions. Additionally, desmoplastic stroma is evident as dense fibrous tissue frequently surrounds the tumor clusters, contributing to a robust and complex microenvironment.
	ILC	Invasive lobular carcinoma (ILC) can be characterized through high-resolution imaging from four distinct perspectives: In single-file arrangement, tumor cells often infiltrate in linear chains between collagen fibers, creating a linear or string-of-beads appearance. In diffuse infiltration, tumor cells spread in a more scattered, non-nodular manner, leading to a less organized and more widespread distribution. There is typically minimal fibroblast activation with fewer myofibroblasts compared to invasive ductal carcinoma (IDC), resulting in a less fibrotic stroma. Additionally, a targetoid pattern may be observed where tumor cells wrap around normal ductal structures, creating a concentric or target-like appearance around these structures.

5. Additional Quantitative Experiments

5.1. Effects of Pathology Foundation Model Encoders

To evaluate the effectiveness of MUSE with different pathology foundation models (FM) serving as feature extractors, we compared four distinct pathological visual-language foundation models, i.e., PLIP [4], MUSK [8], Prov-GigaPath [9], and CONCH [5], under 16-shot setting across ACC, AUC, and F1 Score metrics. The results are presented in Table 2. The results demonstrate that CONCH outperforms other FMs across all evaluation metrics. This stems from CONCH's explicit adoption of a CLIP-style dual-tower architecture [6], which enables effective understanding of pathological text semantics. In contrast, Prov-GigaPath is primarily designed as an image-centric model with self-supervised learning [3]; although it incorporates textual information for fine-tuning, its core remains a unimodal image encoder, thereby limiting its capability in text comprehension.

Table 2. Performance comparison (presented in %) of different foundation models (PLIP, MUSK, Prov-GigaPath, and CONCH) on CAMELYON under 16-shot settings.

FM	ACC	AUC	F1 Score
PLIP [4]	72.82	73.47	67.24
MUSK [8]	86.72	88.28	85.18
Prov-GigaPath [9]	87.32	89.73	84.26
CONCH [5]	**89.70**	**92.52**	**88.59**

5.2. Ablation on the Number of Retrieved Texts

We conduct ablation experiments to investigate the performance across different values of the number of retrieved texts in the SMMO component. The value of this hyperparameter is set to 10, 20, and 80, respectively. The experimental results are presented in Table 3. Under the 16-shot setting, the optimal performance is achieved when the hyperparameter is set to 20. For the 8-shot and 4-shot settings, the best results are obtained with a value of 80. This indicates that in scenarios with sparse visual signals, increasing

Algorithm 1 Training Strategy

Input: Training set of WSI bags $\{B^l\}_{l=1}^{L}$ with labels $\{Y^l\}_{l=1}^{L}$, category text features D, number of experts R, number of selected experts k, top-patch ratio $r\%$, number of retrieved texts m, maximum epoch E_{max}.

Initialize parameters of module DSR, SVTI, and MLP
for epoch $e = 1$ to E_{max} **do**
  for each WSI bag B^l in training set **do**
    // Fine-grained semantic prior f is obtained through the DSR and SVTI modules
    $Q = \text{DSR}(D; k, R)$
    $f = \text{SVTI}(B^l, Q; r\%)$
    $z = \text{MLP}(f)$
    // Retrieve relevant semantics from the category-related text knowledge base
    T_m: The randomly shuffled top m retrieved text features from $\mathcal{B}_{Y^l}$
    for $t \in T_m$ **do**
      $\{Q_j^t\}_{j=1}^{k} = \text{DSR}(t; k, R)$
      $f_{\text{aux}}^t = \text{SVTI}(B^l, \{Q_j^t\}_{j=1}^{k}; r\%)$
      $z_{\text{aux}}^t = \text{MLP}(f_{\text{aux}}^t)$
      $z_{\text{final}}^t = \frac{z + z_{\text{aux}}^t}{2}$
      $\mathcal{L}^t = \text{CrossEntropyLoss}(z_{\text{final}}^t, Y^l)$
      update DSR, SVTI, MLP by back-propagation via Adam W optimizer
    end for
  end for
end for
return Optimal modules DSR*, SVTI*, and MLP*

Algorithm 2 Inference Strategy

Input: Test WSI bag B with label Y, category text features D,optimal modules DSR*, SVTI*, and MLP*.

// Fine-grained semantic prior f is obtained through the DSR and SVTI modules
$Q = \text{DSR}(D; k, R)$
$f = \text{SVTI}(B, Q; r\%)$
$z = \text{MLP}(f)$
// Label prediction via argmax over logit
$\hat{y} = \text{argmax}(z)$
return predicted label $\hat{y}$

semantic diversity contributes to improved model generalization.

5.3. Sensitivity to the Number of Experts

To investigate the sensitivity of model performance to the number of experts in the DSR module, we conducted experiments with the number of experts set to 4, 8, and 16, while consistently selecting the top-2 experts based on gating scores. As shown in Table 4, the experimental results demonstrate that 8-experts achieves the best performance under the 16-shot setting, while 4-experts yield the optimal results in the 4-shot setting.

Table 3. Performance comparison (presented in %) of different number of retrieved texts on CAMELYON under few-shot learning settings.

	number of retrieved texts	ACC	AUC	F1 Score
16-shot	10	87.88	91.33	86.75
	20	**89.70**	**92.52**	**88.59**
	80	88.43	91.63	87.26
8-shot	10	83.64	86.44	80.79
	20	84.01	88.32	82.42
	80	**84.49**	**88.40**	**83.07**
4-shot	10	69.14	71.41	64.01
	20	74.86	76.65	68.66
	80	**77.32**	**77.95**	**72.53**

Table 4. Performance comparison (presented in %) of different number of experts on CAMELYON under few-shot learning settings.

	number of experts	ACC	AUC	F1 Score
16-shot	4	87.91	90.38	86.64
	8	**89.70**	**92.52**	**88.59**
	16	87.32	90.16	86.18
8-shot	4	82.88	87.49	81.52
	8	84.01	**88.32**	**82.42**
	16	**84.31**	87.60	81.94
4-shot	4	**75.31**	**77.43**	**68.90**
	8	74.86	76.65	68.66
	16	72.49	75.01	68.27

5.4. Ablation on the Top-Patch Ratio

We compare different top-patch ratios in DSR module to investigate the impact of this hyperparameter on model performance. We set the top-patch ratios to 10%, 20%, 50%, and 100% (retaining all patches), and conducted experiments on CAMELYON under 16-shot, 8-shot, and 4-shot settings. The results are presented in Table 5. The results show that interacting with a subset of patches at an appropriate ratio yields better performance than retaining all patches. This indicates that adopting an appropriate top-patch ratio can effectively suppress the substantial redundant noise inherent in patches, thereby enhancing the discriminability of the interacted patch representations.

Table 5. Performance comparison (presented in %) of different top-patch ratio on CAMELYON under few-shot learning settings.

	Ratio	ACC	AUC	F1 Score
16-shot	10%	88.92	91.92	87.83
	20%	**89.70**	**92.52**	**88.59**
	50%	88.51	91.66	87.40
	100%	88.51	91.62	87.53
8-shot	10%	85.65	88.58	83.65
	20%	84.01	88.32	82.42
	50%	**85.57**	**90.82**	**84.28**
	100%	84.34	86.98	82.54
4-shot	10%	71.15	73.25	67.26
	20%	**74.86**	**76.65**	**68.66**
	50%	70.89	72.72	62.34
	100%	69.10	70.17	62.97

6. Evaluation at Higher Shot Counts

We evaluate MUSE against pure vision MIL (ABMIL, TransMIL) and VLM baselines (ViLa-MIL, FOCUS) using AUC at higher shot count (32- and 64-shot) on CAMELYON, as shown in Figure 1. MUSE still achieves the best performance at 32- (93.23%) and 64-shot (95.00%), though semantic gains diminish as visual samples increase. This underscores that semantic priors hold greatest potential under data scarcity—exactly in the standard few-shot settings (4-/8-/16-shot) that our work focuses on.

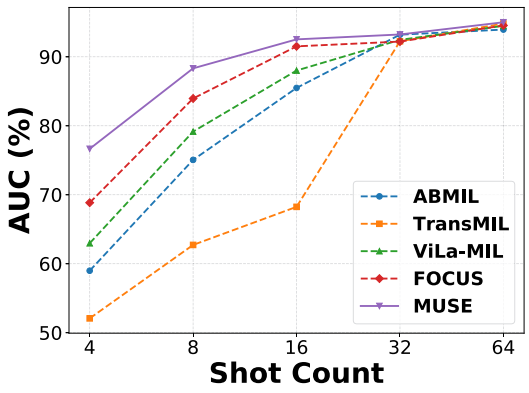

Figure 1. Evaluation of model performance under higher-shot settings (32- and 64-shot) on CAMELYON

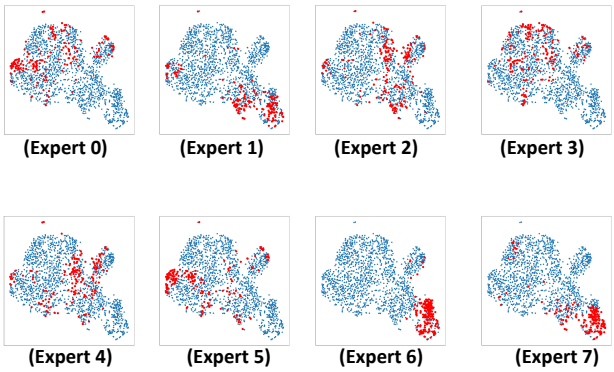

Figure 2. Visualization of the regions attended by individual experts.

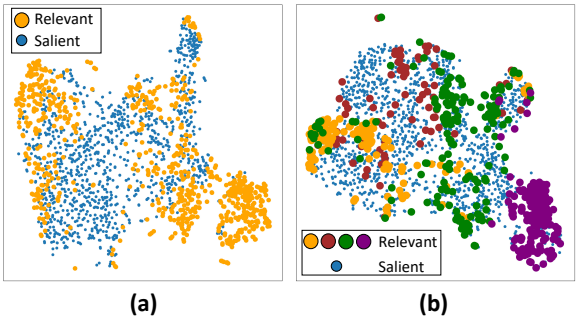

Figure 3. The visualization analysis of semantic refinement via DSR. (a) Visual regions associated with text mapping through the cross-attention mechanism. (b) Relevant visual regions after mapping via DSR.

7. Additional Visualization

7.1. Visualization of Attended Patch Features by Experts

To intuitively analyze the relationship between the semantic knowledge decomposed by each expert and the patch features, we compute the similarity between the semantic information processed by each expert and the key projections derived from the patch features. We then select the top-20% of patches based on their similarity scores and highlight the value projections obtained from these patches. As shown in Figure 2, this visualization reveals the specific regions attended by each expert. The visualization results demonstrate that different experts attend to distinct aspects of the patch features, indicating specialization in capturing diverse semantic patterns.

To visually demonstrate the semantic refinement decomposition achieved by DSR and its corresponding alignment with visual features, we provide the visualization analysis as shown in Figure 3. The comparisons demonstrate that, compared to cross-attention, DSR enables fine-grained semantic modeling and focuses on more concentrated regions.

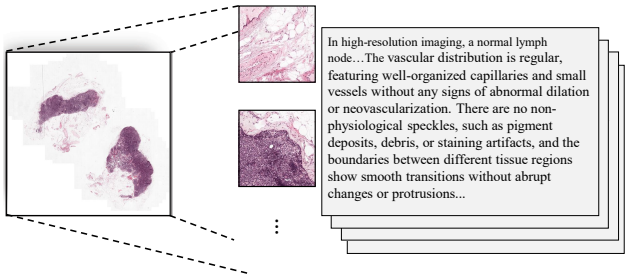

Figure 4. Retrieved textual descriptions from the knowledge base given a WSI query.

7.2. Semantic Retrieval Results for one WSI Instance

We select WSI normal_001 in CAMELYON 16 as the query to retrieve the corresponding textual descriptions from the knowledge base, as shown in Figure 4. This indicates that the retrieved textual descriptions are consistent with the image characteristics of the WSI.

8. Limitation

Although the DSR module aligns fine-grained semantics with patch features by leveraging the Mixture-of-Experts for refined semantic modeling, performance improvements on the benchmark alone, along with qualitative visualizations, are insufficient to fully validate its interpretability. Specifically, we do not employ stronger inductive biases to enforce specialization among the experts, but rather rely solely on data-driven adaptation to guide their learning. This limitation highlights a promising direction for future research: incorporating informative priors to constrain the learning process of experts, thereby enhancing the interpretability of semantic perception.

9. Examples generated by LLM for CAMELYON

We utilize GPT-4 to generate 10 examples of descriptions for each category in CAMELYON, covering four aspects (Cellular morphology, Tissue architecture, Color-staining, and Spatial-texture pattern), as shown on the following pages.

References

[1] Josh Achiam, Steven Adler, Sandhini Agarwal, Lama Ahmad, Ilge Akkaya, Florencia Leoni Aleman, Diogo Almeida, Janko Altenschmidt, Sam Altman, Shyamal Anadkat, et al. Gpt-4 technical report. *arXiv preprint arXiv:2303.08774*, 2023. 1

[2] Kingma DP Ba J Adam et al. A method for stochastic optimization. *arXiv preprint arXiv:1412.6980*, 1412 (6), 2014. 1

[3] Kaiming He, Xinlei Chen, Saining Xie, Yanghao Li, Piotr Dollár, and Ross Girshick. Masked autoencoders are scalable vision learners. In *Proceedings of the IEEE/CVF conference on computer vision and pattern recognition*, pages 16000–16009, 2022. 2

[4] Zhi Huang, Federico Bianchi, Mert Yuksekgonul, Thomas J Montine, and James Zou. A visual–language foundation model for pathology image analysis using medical twitter. *Nature medicine*, 29(9):2307–2316, 2023. 2

[5] Ming Y Lu, Bowen Chen, Drew FK Williamson, Richard J Chen, Ivy Liang, Tong Ding, Guillaume Jaume, Igor Odintsov, Long Phi Le, Georg Gerber, et al. A visual-language foundation model for computational pathology. *Nature medicine*, 30(3):863–874, 2024. 2

[6] Alec Radford, Jong Wook Kim, Chris Hallacy, Aditya Ramesh, Gabriel Goh, Sandhini Agarwal, Girish Sastry, Amanda Askell, Pamela Mishkin, Jack Clark, et al. Learning transferable visual models from natural language supervision. In *International conference on machine learning*, pages 8748–8763. PmLR, 2021. 2

[7] Laurens van der Maaten and Geoffrey Hinton. Visualizing data using t-sne. *Journal of Machine Learning Research*, 9(86):2579–2605, 2008. 1

[8] Jinxi Xiang, Xiyue Wang, Xiaoming Zhang, Yinghua Xi, Feyisope Eweje, Yijiang Chen, Yuchen Li, Colin Bergstrom, Matthew Gopaulchan, Ted Kim, et al. A vision–language foundation model for precision oncology. *Nature*, 638(8051):769–778, 2025. 2

[9] Hanwen Xu, Naoto Usuyama, Jaspreet Bagga, Sheng Zhang, Rajesh Rao, Tristan Naumann, Cliff Wong, Zelalem Gero, Javier González, Yu Gu, et al. A whole-slide foundation model for digital pathology from real-world data. *Nature*, 630(8015):181–188, 2024. 2

CAMELYON(Normal)
(Cellular morphology)

Examples:

•Uniform cell size: Most lymphocytes are small and similar in size
•Round or oval nuclei: Nuclei are generally round or slightly oval with clear boundaries.
•Consistent staining: Nuclei stain deep purple (basophilic), and cytoplasm is light pink.
• High nuclear-to-cytoplasm ratio: Nuclei are large relative to cytoplasm, but consistent across cells.
•Even nuclear chromatin: Nuclear staining is homogeneous without coarse granularity or heterogeneity.
•Regular nuclear distribution: Cells are densely packed but organized, without crowding or clustering.
•Absence of nuclear atypia: No multinucleation, irregular nuclear shapes, or abnormal mitotic figures.
•Clear cell boundaries: Adjacent cells are well-demarcated, without fusion or overlap.
•No atypical cell clusters: No groups of morphologically abnormal cells are present.
•Intact tissue architecture: Follicles, cortex, and medulla are clearly defined, and cellular arrangement follows normal physiological patterns.

CAMELYON (Normal)
(Tissue architecture)

Examples:

- Intact capsule: a well-defined connective tissue boundary surrounding the lymph node.
- Clear cortex structure: dense cortical regions with uniformly arranged lymphoid follicles.
- Normal medulla: orderly medullary cords and open sinuses without disruptive lesions.
- Regular follicles: round or oval in shape, with pale germinal centers in the middle.
- Open lymphatic sinuses: sinusoids are patent, containing scattered lymphocytes or macrophages but no dense infiltrates.
- Normal vascular distribution: capillaries and small vessels are regularly arranged, without abnormal dilation or neovascularization.
- Clear interfollicular regions: uniform stromal fibers without fibrosis or necrosis.
- Even lymphocyte density: lymphocytes are evenly distributed in both cortex and medulla, with no abnormal clustering or voids.
- Absence of abnormal cell clusters: no atypical cells, nuclear enlargement, or necrotic foci.
- Uniform staining: consistent H&E coloration, with pink cytoplasm and dark purple nuclei, and no obvious blotches or unstained areas.

CAMELYON(Normal)
(Color-staining)

Examples:

- Nuclei stained blue-purple: Hematoxylin imparts a uniform blue-purple color to cell nuclei with clear edges.
- Cytoplasm stained pink: Eosin colors most cytoplasm in light pink or pale red.
- Clear tissue structures: Distinct demarcation of follicles, sinusoids, and lymphocyte-rich versus stromal areas lymphocyte-rich versus stromal areas.
- Uniform color distribution: Regions of the same tissue type show consistent staining intensity without blotches.
- No abnormal dark red or deep purple regions: Absence of excessive blood, necrosis, or hemorrhage.
- Connective tissue lightly stained: Collagen and fibrous tissue appear in pale pink or light blue.
- Normal blood cell color in vessels: Red blood cells appear orange-red, and vessel outlines are clear.
- Lightly stained follicle centers: Germinal centers and follicle cores appear pale pink or light blue.
- Even coloration in lymphocyte-rich areas: Dense lymphocyte zones are uniformly blue-purple without localized dark spots.
- No non-physiological speckles: Absence of pigment deposits, debris, or staining artifacts.

CAMELYON(Normal)
(Spatial-texture pattern)

Examples:

•Uniform follicle distribution: Lymphoid follicles are consistent in size, orderly arranged, with clear boundaries.
•Regular sinus structures: Lymphatic sinuses form a mesh-like or radiating pattern, maintaining normal patency without abnormal dilation.
•Even cell density: Lymphocytes are distributed uniformly, without localized overcrowding or sparsity.
•Consistent staining intensity: H&E staining is uniform; nuclei appear blue-purple and cytoplasm pink, with no obvious color blotches.
•Ordered cortex and medulla architecture: Cortical, medullary, and marginal regions are clearly delineated and layered.
•Smooth boundary transitions: Transitions between tissue regions are natural, without abrupt changes or protrusions.
•Regular vascular and small duct orientation: Blood vessels and small ducts are slender, orderly, and follow natural paths without abnormal dilation or breaks.
•Absence of abnormal masses or cavities: Tissue textures are continuous, without noticeable voids or nodular formations.
•Stable texture orientation: Fibrous connective tissue and lymphocyte arrangements follow natural orientation without abrupt directional changes.
•Low local noise: Cell distribution and tissue texture lack isolated artifacts or abnormally bright spots.

CAMELYON(Tumor)
(Cellular morphology)

Examples:

•Nuclear enlargement: tumor cells often have larger nuclei compared to normal lymphocytes.
•Irregular nuclear shape: nuclei may appear pleomorphic or misshapen.
•Hyperchromasia: nuclei show increased staining intensity due to dense chromatin.
•High nuclear-to-cytoplasmic ratio: the nucleus occupies a larger portion of the cell.
•Prominent nucleoli: visible, enlarged nucleoli within nuclei.
•Increased mitotic figures: higher number of cells undergoing division.
•Loss of normal cell polarity: disorganized orientation of cells within tissue.
•Cellular crowding: densely packed cells, often forming clusters or sheets.
•Anisocytosis: variability in cell size across the tissue.
•Nuclear membrane irregularities: irregular or indented nuclear borders.

CAMELYON(Tumor)
(Tissue architecture)

Examples:

•Disrupted lymph node capsule: the outer boundary of the lymph node is breached by tumor cells.
•Loss of normal follicular structure: lymphoid follicles appear distorted or absent.
•Sinusoidal dilation or obstruction: lymphatic sinuses are enlarged or filled with tumor cells.
•Replacement of normal parenchyma: normal lymph node tissue is replaced by sheets of tumor cells.
•Infiltrative growth patterns: tumor cells infiltrate surrounding stromal tissue irregularly.
•Heterogeneous tissue density: uneven distribution of cellular and extracellular regions.
•Formation of micrometastatic clusters: small aggregates of tumor cells scattered throughout the node.
•Necrotic areas within tissue: localized cell death due to tumor proliferation.
•Fibrotic or desmoplastic response: abnormal connective tissue growth around tumor regions.
•Irregular or distorted vascular structures: blood vessels within the lymph node are compressed, dilated, or irregularly branched.

CAMELYON(Tumor)
(Color-staining)

Examples:

•Increased nuclear basophilia: darker purple nuclei due to higher DNA content in tumor cells.
•Hyperchromatic nuclei: nuclei appear more intensely stained than in normal tissue.
•Pale or eosinophilic cytoplasm: abnormal cells may show lighter pink cytoplasm compared to surrounding lymphocytes.
•Uneven H&E staining: irregular staining intensity across tumor regions.
•Prominent nucleoli: nucleoli stained intensely, appearing as bright spots within nuclei.
•High nucleus-to-cytoplasm (N/C) ratio: more purple nuclear staining relative to cytoplasm.
•Diffuse or patchy staining patterns: loss of normal tissue color homogeneity.
•Presence of necrotic areas: pale or ghost-like regions with faint staining.
•Dark clusters of tumor cells: concentrated, intensely stained regions indicating dense metastases.
•Altered stromal staining: surrounding stroma may appear more pink or irregularly colored due to reactive changes or fibrosis.

CAMELYON(Tumor)
(Spatial-texture pattern)

Examples:

•Irregular clustering of tumor cells disrupting normal tissue organization.
•High cellular density regions compared to surrounding normal lymphoid tissue.
•Loss of normal follicular or sinusoidal structures in affected areas.
•Heterogeneous texture patterns with abrupt transitions between normal and abnormal regions.
•Streaks or nests of tumor cells forming elongated or irregular shapes.
•Patchy or fragmented tumor regions scattered within otherwise normal tissue.
•Diffuse infiltration patterns, where tumor cells spread along existing tissue frameworks.
•Sharp contrast in color intensity and texture between tumor and adjacent stroma.
•Micro-metastatic foci appearing as small, isolated clusters with distinct textures.
•Distorted vascular or connective tissue patterns due to tumor invasion.